INTERNATIONAL JOURNAL FOR NUMERICAL METHODS IN FLUIDS, VOL. 8, 1563–1586 (1988)

FINITE ELEMENT SIMULATION OF 3D TURBULENT FREE SHEAR FLOWS*

DOMINIQUE PELLETIER AND RICARDO CAMAREO

Computational Engineering Group, Applied Mathematics Department, Ecole Polytechnique de Montreal, P.O. Box 6079, Station 'A', Montreal, Canada H3C 3A7

SUMMARY

This paper reviews past and current efforts in developing a simple but robust turbulence model for free shear flows. Much of this work has been published previously and this paper is a rearrangement aimed at the conference. The model is presented and is interfaced with FIDAP to solve three-dimensional flows and a pusher—prop configuration. The eight-node brick, the penalty formulation and the Broyden method are used to solve the Navier–Stokes equations. The propeller is modelled as an actuator disc and the direct simulation of a given propeller is considered in detail. Good results are obtained for the square jet. For propeller cases detailed comparison with wind tunnel measurements shows excellent prediction of the velocity and pressure for flows of this complexity.

KEY WORDS Finite element Turbulence model Free shear flows

INTRODUCTION

Detailed analysis of the three-dimensional flow produced by propeller–body combinations is of interest for a number of practical applications and scientific issues. Examples include the influence of the propeller on the body pressure distribution, the prediction of the near-wake profile, cyclic loading that produces vibrations and the influence of a downstream surface on a propeller and vice versa. The scientific issues mainly concern the nature of turbulence and turbulence modelling for such flows, 3D grid generation and numerical methods for the full, 3D, Reynolds-averaged Navier–Stokes equations. This paper focuses on the turbulence modelling and the numerical aspects of the solution process.

Until recently only approximate analytical or numerical treatments of propeller flowfields were available involving one or more of the following very restrictive assumptions: the flow was assumed inviscid or laminar; the propeller was represented as an actuator disc with constant thrust and torque over the disc area; the effects of the propeller on the flowfield were assumed small enough to permit linearization of the equations of motion. References 1–8 are representative. Some workers have suggested the use of parabolic formulations, but that seems questionable as a result of the well known 'upstream influence' of propellers which implies an elliptic mathematical behaviour.

The numerical procedure reported in References 9 and 10 had as its goal the development of a realistic treatment, keeping simplifying assumptions and approximations to a minimum. The

* Presented at the 1st FIDAP Users Conference, Evanston, Illinois, U.S.A., 13–15 September 1987.

0271–2091/88/121563–24$12.00

Received 7 December 1987
Received 14 July 1988

work was based on the full, unsteady, Reynolds-averaged Navier–Stokes equations. To place some bounds on the scope of the effort at the time, however, some simplifications were necessary. The first was the assumption of an actuator disc model for the propeller, although arbitrary radial variations of thrust and torque were allowed. Secondly, the flow was taken as axisymmetric. Thirdly, turbulent transport processes were described by an integrated, turbulence kinetic energy (TKE) model, which was used to predict an eddy viscosity. The unsteady equations of motion were cast in terms of a streamfunction, one vorticity component and the peripheral velocity. The equations were solved by an ADI finite difference method. Comparison of the predictions with the laboratory data showed good agreement for the axial velocity. The swirl predictions were consistently low.

For applications to problems of practical interest the most severe limitation to the analysis described above was its restriction to two-dimensional axisymmetric flows. Actual propeller-driven vehicles have either a three-dimensional body near the propeller and/or appendages that render the flow three-dimensional. For many cases the assumption of an actuator disc representation of the propeller remains appropriate while the restriction to axisymmetric flow does not. Furthermore, the jump to trying to treat the viscous, three-dimensional, cyclically unsteady problem with individual blades and their boundary layers is too great to attempt in one step at this time.

The present work is part of a step-by-step approach to the development of a computational method for the analysis of propeller flowfields with three-dimensional inflows and the effect of hull and appendages in configurations of increasing complexity and realism. The fully elliptic, 3D, time-averaged, steady Navier–Stokes equations are solved with FIDAP by a penalty finite element method. This approach allows for ease of handling complex geometries and a variety of boundary conditions. Turbulence modelling is done through generalizations of the integrated TKE model of References 9–11.

ANALYSIS

Equations of motion

The Boussinesq form of the time-averaged Navier–Stokes equations is given by

$$U_{i,i} = 0, \tag{1}$$

$$\rho U_j U_{i,j} = -P_{,i} + \rho f_i + [\mu_T (U_{1,j} + U_{j,i}]_{,j}, \tag{2}$$

where μ_T is a turbulent eddy viscosity and f_i are local body forces that will model the effects of the propeller and screen disc.

Turbulence model

A good turbulence model should respond to all important flow processes anticipated, but it should not complicate the mathematical formulation nor burden the computational task more than is absolutely necessary. This last point is especially important for large-scale, three-dimensional simulations.

The starting point for the development of the present model is the transport equation for the turbulence kinetic energy model:[12]

$$U_i k,^i = (\nu_T/\sigma_T k_{,i})_{,i} + \nu_T (U_{i,j} + U_{j,i}) U_{i,j} - \varepsilon.$$

Summation over repeated indices is implied; the comma denotes partial differentiation. In this

equation ν_T is the kinematic eddy viscosity, σ_T is a turbulence 'Prandtl' number and ε is the viscous dissipation of turbulence. This equation is the high-Reynolds-number form of the TKE equation; it is suitable for the present application since there are no solid walls in the computational domain. The left-hand side represents convection of k, while the first, second and third terms on the right-hand side represent diffusion, production and viscous dissipation respectively.

For the flows considered in this study, the fully elliptic form of the TKE equation is not required. Indeed, a parabolized form is sufficient since it is expected that the turbulence level at one point will not be significantly affected by turbulence levels at the points located further downstream. The parabolized form of the TKE equation is obtained by neglecting streamwise diffusion, production due to normal turbulent stresses and terms involving streamwise or x-derivatives. Thus we have

$$Uk_{,x}+Vk_{,y}+Wk_{,z}=(\nu_T/\sigma_T k_{,y})_{,y}+(\nu_T/\sigma_T k_{,z})_{,z}+\nu_T[U_{,y})^2+(U_{,z})^2+(V_{,z}+W_{,y})^2-\varepsilon.$$

Following References 9 and 10, an integrated form of this last equation is obtained by integrating it over the cross-sectional y–z plane normal to the primary direction of the flow. Application of the divergence theorem to the second and third terms on the left-hand side and to the diffusion terms on the right-hand side makes them formally disappear upon integration if k and its crossflow partial derivatives vanish laterally in the far field. After some algebraic manipulations, the TKE equation reads

$$\mathrm{d}\left(\iint_A \rho Uk\,\mathrm{d}A\right)\Big/\mathrm{d}x=\iint_A \nu_T[U_{,y})^2+(E_{,z})^2+(V_{,z}+W_{,y})^2]\,\mathrm{d}A-\iint_A \varepsilon\,\mathrm{d}A. \tag{3}$$

In order to close the model, the TKE is related to the eddy viscosity by the Prandtl–Kolmogorov relationship:

$$\mu_T=\rho\nu_T=c_2 k^{1/2}L. \tag{4}$$

As usual[12] one takes

$$\varepsilon=a_2 k^{3/2}/L, \tag{5}$$

where L is a length scale of the shear layer and a_2 and c_2 are constants. Physically the flow field variables are sufficiently well behaved to ensure boundedness of the integrals in equation (3). The assumption that the eddy viscosity is constant over the cross-section of the flow is a well documented behaviour for free shear flows. In fact, close scrutiny of the available experimental data reveals that the eddy viscosity is constant over most of the cross-section of the shear layer and decays to zero only as the radial distance r from the x-axis goes to infinity. To preserve this behaviour and ensure boundedness of the integrals in the modelled integrated equation, a distribution function γ, representing the distribution of the eddy viscosity across the layer, is introduced. The following equation (whose functional form was suggested in Reference 13), obtained from a non-linear least-squares fit to intermittency data for a turbulent boundary layer over a flat plate and turbulent round and planar jets,[13,14] was found to be satisfactory:

$$\gamma=\gamma_y\gamma_z,$$

where

$$\gamma_y=0{\cdot}5[1-\mathrm{erf}(1{\cdot}98\,Y/Y_{1/2}-3{\cdot}42)],$$

$$\gamma_z=0{\cdot}5\,[1-\mathrm{erf}(1{\cdot}98\,Z/Z_{1/2}-3{\cdot}42)].$$

The half-widths are defined by the points on the Y- and Z-axes where

$$(U-U_\infty)/(U-U_\infty)_{\max}=0{\cdot}5. \tag{6}$$

In this expression U_∞ is the free stream approach flow velocity, which can be non-uniform. It should be noted that the particular form of the distribution is not critical. Its purpose is to ensure boundedness of the integrals. Choosing different forms results in slightly different values of the constants a_2 and c_2 when the model is calibrated.[15] This will not affect the performance of the turbulence model.[15]

Upon substitution of equations (4) and (5) into equation (3) the modelled integrated TKE equation becomes

$$\mathrm{d}\nu_T/\mathrm{d}x = 0{\cdot}5(Y_2 - \nu_T\,\mathrm{d}Y_1/\mathrm{d}x - \nu_T^2 Y_3)/Y_1, \tag{7}$$

where

$$Y_1 = \iint_A (U\gamma^2/c_2L^2)\,\mathrm{d}A, \tag{8}$$

$$Y_2 = \iint_A \gamma[(U_{,y})^2 + (U_{,z})^2 + (V_{,z} + W_{,y})^2]\,\mathrm{d}A, \tag{9}$$

$$Y_3 = \iint_A (\gamma a^2/c_2^3L^4)\,\mathrm{d}A. \tag{10}$$

Following Reference 16

$$L = [(Y_{1/2}^a Z_{1/2}^a)/(Y_{1/2}^a + Z_{1/2}^a)]^{1/a}.$$

This choice for the length scale ensures correct dependence for both limiting cases of planar and axisymmetric jet flows.[16] This is crucial for three-dimensional jet flows since both regimes are present.[17]

Equation (7) is an initial value problem for the eddy viscosity. The only data required to solve equation (7) is an initial condition for the eddy viscosity, a value that can easily be estimated for most flows. A significant advantage of the present model is the absence of the diffusion of TKE, a very difficult term to model.

The model was calibrated[15] on the simple, well documented turbulent flow problem of the far field of a round jet issuing into still surroundings. This flow has an analytical solution for the velocity field and the eddy viscosity is a known constant.[18] The integrals are evaluated exactly and with the assumption of turbulence equilibrium the constants are determined to be

$$a_2 = 0{\cdot}519, \qquad c_2 = 0{\cdot}154.$$

These values of the constant are expected to be valid for propeller flows since the turbulence in such flows is very similar to that of round jets.[14]

SOLUTION ALGORITHM

The turbulence model was programmed and interfaced with the general purpose finite element program FIDAP for incompressible flows.

Interfacing the turbulence model with FIDAP

One of the goals during the FORTRAN implementation of the turbulence model was to minimize the number of patches that had to be made on FIDAP. One must recall that this work started in 1981 while FIDAP was at version 0·0 of its commercial life! Several updates and revisions were expected to follow at a relatively quick pace, and since our goal was to solve

turbulent free shear flows, minimization of the programming task to follow the changes of FIDAP was of prime importance.

The turbulence model was programmed as a separate set of subroutines. The driving routine EDDY3D controls all phases of the turbulence model solution process: input of the various control parameters for the model, input of the topology of the cross-section of the flowfields, computation of the various integrals, interpolation and differentiation of the integral coefficient and solution of the ODE problem.

Integrals in equations (8)–(10) are evaluated with the finite element methodology. A cross-section of the mesh is represented by surface elements and integrals over elements of a section are summed. Element integrals are evaluated using Gaussian integration.

The length scales are computed by extracting the velocity field on each side of the Y- and Z-axes at each station, computing the velocity defect equation (6) on each axis and performing an inverse interpolation to find the point defined by equation (6).

The ODE problem of equation (7) is solved using the subroutine DVERK from the IMSL library. Since DVERK requires evaluation of the right-hand side of equation (7) at axial locations other than those defined by the grid, the values of the integrals were spline fitted for easy interpolation and differentiation by the IMSL cubic spline routines.

All arrays for the integrals, their spline representation and work arrays were stored in named commons independent of FIDAP's organization. It should be noted that for solving the turbulence model one must have access to the global velocity field and nodal co-ordinates. Scratch space had to be allocated to recover FIDAP's arrays IDE(i, j) of equation numbers, X, Y and Z of co-ordinates and arrays for the three velocity component nodal vectors **U**, **V**, **W**. This space had to be allocated separately in a named common, since when the turbulence subroutine is first called, FIDAP has already entered its own equation-solving phase and no memory is available in the blank common.

With this approach only two subroutines of FIDAP had to be modified. First, a call to EDDY3D was inserted in FIDAP's routine ELRESF which computes element stiffness matrices, residuals and forces. Secondly, the routine VS3MDL to compute the fluid viscosity at the Gaussian points was modified to include interpolation from the eddy viscosity data provided by EDDY3D. The information is extracted from the appropriate commons and IMSL routines are used to perform the interpolation.

These modifications were implemented so as to preserve all the built-in flexibility offered by the FIDAP package. Mixed and penalty formulations can be used. Steady and transient analyses are possible with explicit and implicit integrators. All non-linear equation solvers can be used (successive substitution, Newton–Raphson and quasi-Newton).

General solution procedure

For reasons of economy, the equations of motion are discretized in a penalty formulation with an eight-noded brick with trilinear velocity and discontinuous piecewise constant pressure. Details of the penalty Galerkin formulation can be found in the FIDAP users' manual. While this element, under certain circumstances, may suffer from spurious pressure solutions, our experience indicates that it is a robust and reliable element for the problems treated here.

The resulting system of non-linear equations is solved by the quasi-Newton method with Broyden updata. The user of this solver resulted in substantial computational savings for a given tolerance of the global iteration scheme. The following iteration strategy was found to be suitable: starting from a first guess of the velocity field (usually an axisymmetric solution, also obtained with FIDAP), the quasi-Newton method is used to iterate until convergence. The eddy viscosity

distribution is updated at each iteration by solving equation (6) using the current velocity field distribution to evaluate the coefficients of the ODE.

The resulting code can simulate planar, axisymmetric and three-dimensional turbulent free shear flows.

Non-dimensionalization

All calculations were performed with a non-dimensional form of the equations of motion. Reference values are selected for the velocity U_0 and pressure P_0 to obtain the following dimensionless variables (the star denotes a dimensional variable):

$$x_i = x_i^*/L_0, \qquad U_i = U_i^*/U_0^*, \qquad P = (P^* - P_0^*)/(\rho^* U_0^{*2}),$$
$$\mu_T = \mu_T/(\rho^* U_0^* L_0^*), \qquad f = f^*/(U_0^{*2}/L_0^*), \qquad \rho = \rho^*/\rho_0^* = 1.$$

RESULTS AND DISCUSSION

The square jet[19]

This is a good first test case for the present model. Although the flow is truly three-dimensional, the far field of the square jet reverts to that of a round jet (on which the turbulence model was calibrated) into still surroundings and the numerical solution in that region should be very close to that of the round jet.

The equations of motion were non-dimensionalized with the jet velocity at the lips (50 ft s^{-1}) and the nozzle half-width (0.25 in). A grid of eight-noded brick elements was used to model one quarter of the jet; see Figure 1. It has 14 elements in the axial direction and 10 elements in the y- and z-directions. The experimental values of the axial velocity component from Reference 19 are used in the nozzle; the transverse velocity components are set to zero. A no-slip condition is used along the wall and symmetry is enforced on the (x, y) an (x, z) planes of symmetry. On the free boundaries U is set to zero and the two remaining components of the traction are set to zero. At the outflow all tractions are set to zero.

A value of the eddy viscosity is needed to initialize the ordinary differential equation governing the eddy viscosity distribution. This is obtained from a simple analysis for jets.[20] Throughout the potential core[20] this analysis yields

$$\nu_T = 0{\cdot}0137\, U_{jet}\, x,$$

where U_{jet} is the jet exit velocity and x is the distance from the lips of the jet. The extent of the potential core may be estimated with the following formula:[24]

$$x_c^*/D = 2{\cdot}13\,(Re_D)^{0{\cdot}097},$$

where x_c^* is the length of the potential core, D is the hydraulic diameter of the jet and Re_D is the Reynolds number based on the jet diameter and the exit velocity. The above formula gives the distribution of the eddy viscosity throughout the potential core of the jet. The value computed at x_c is used to initialize the integrated turbulence model which is then used to compute the distribution of eddy viscosity from the end of the potential core to the outflow boundary of the domain.

Figure 2 presents the dimensionless eddy viscosity distribution as a function of x. The initial linear segment corresponds to the potential core approximation. From there on the high velocity gradients cause high production levels in the integrated TKE model, resulting in a rapid increase

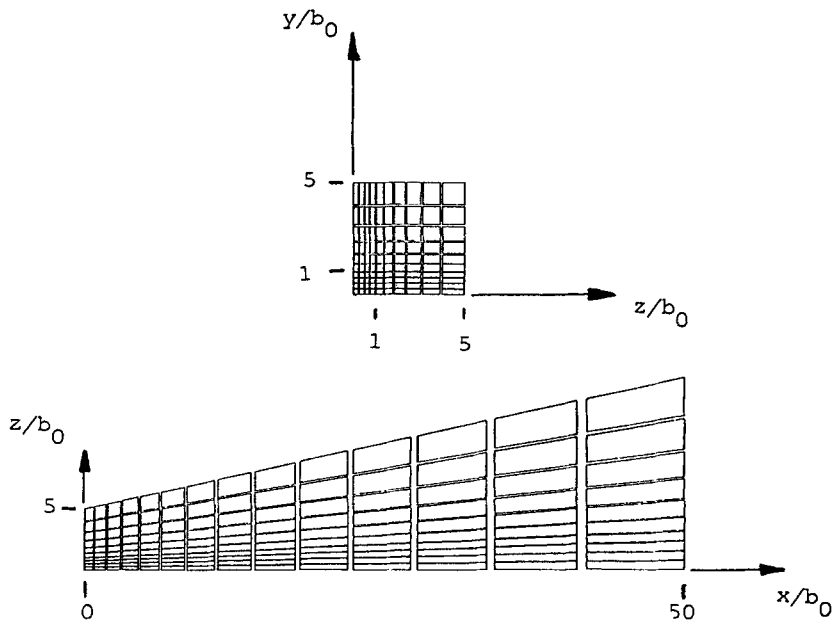

Figure 1. Finite element mesh for the square jet

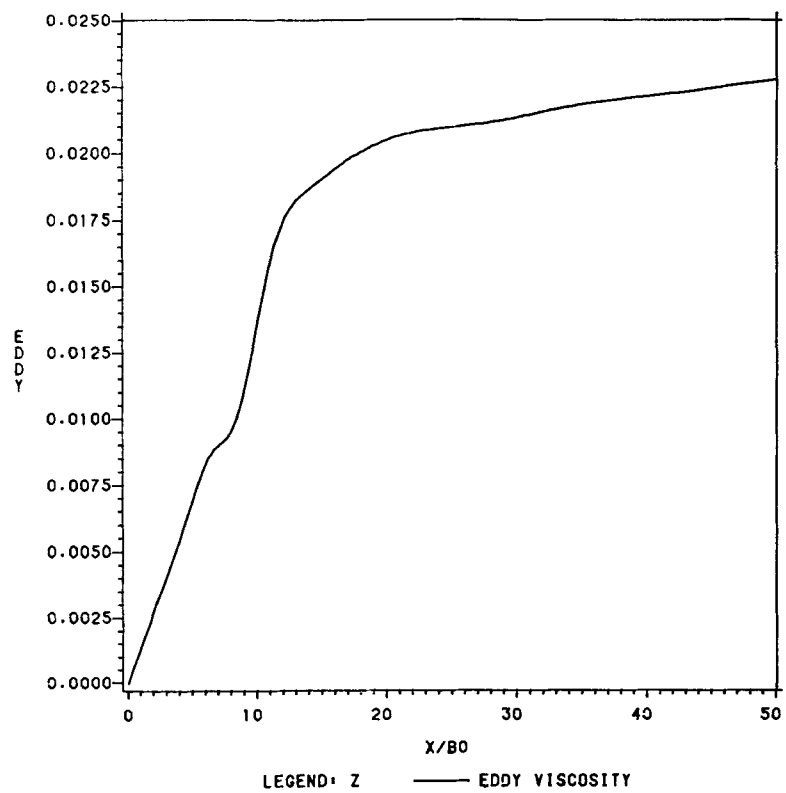

Figure 2. Eddy viscosity for the square jet

of the eddy viscosity downstream of the potential core. The eddy viscosity then tends asymptotically to the analytical value for the round jet, as expected.[20] Far enough downstream of the jet lips, all jets of non-circular section tend towards the round jet far-field behaviour. For the present simulation the domain does not extend far enough downstream to allow the jet to revert completely to the axisymmetric regime.

Figure 3 compares the predicted and experimental centreline velocity distributions. Agreement with the data is excellent. Figure 4 illustrates the predicted and experimental half-width of the jet. The near-field values are not quite constant, as one would expect. This is probably due to the use of a one-layer model, a rather crude approximation for the complicated flow near the lips of the jet.

Figure 5 presents pressure contour plots at two axial stations. They clearly illustrate the three-dimensional nature of the flow and the transition to round jet behaviour far downstream. The top plot is taken at $x/b_0 = 1{\cdot}85$, close to the lips of the jet. The sharp corners in the pressure contours clearly indicate the effect of the shape of the jet lips on the near field. The bottom plot, taken at $x/b_0 = 27$, shows an almost perfectly axisymmetric pressure field, characteristic of the round jet.

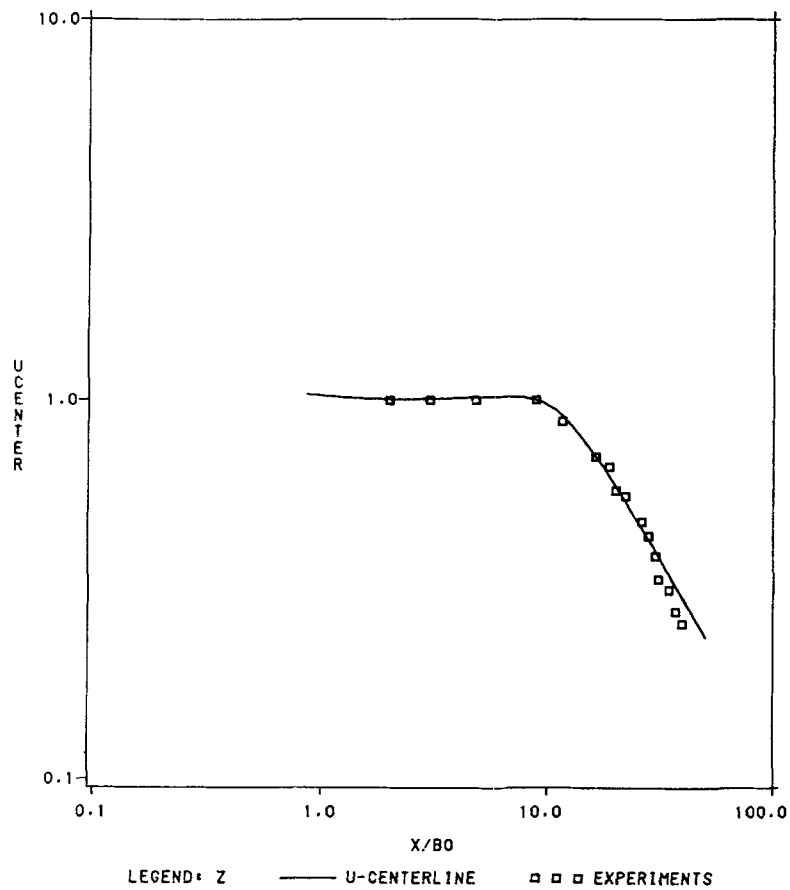

Figure 3. Centreline velocity for the square jet

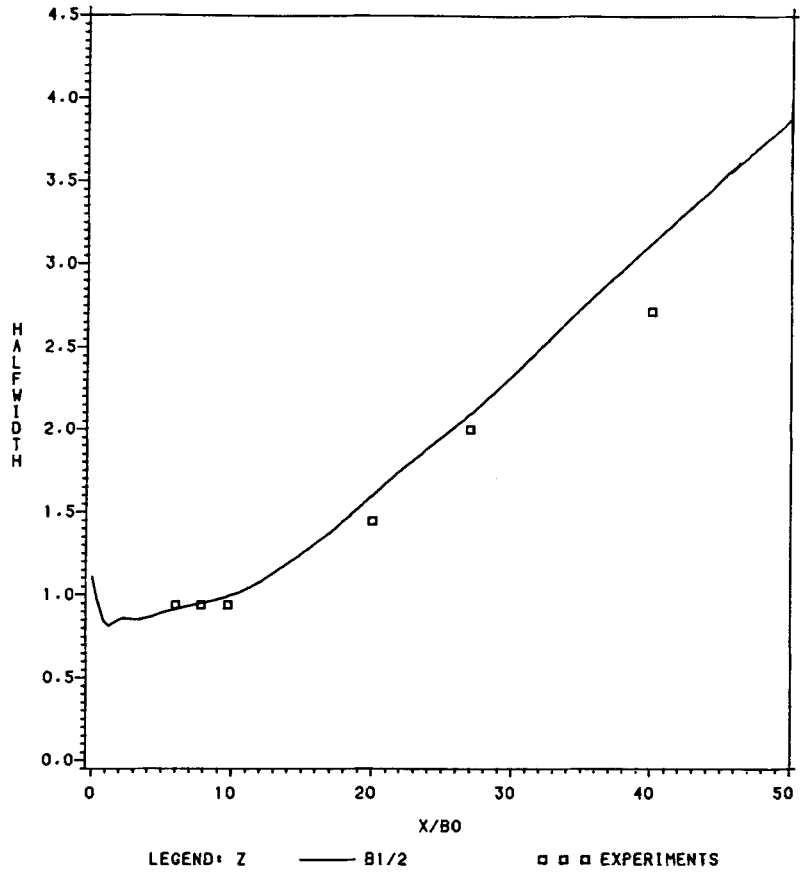

Figure 4. Half-width for the square jet

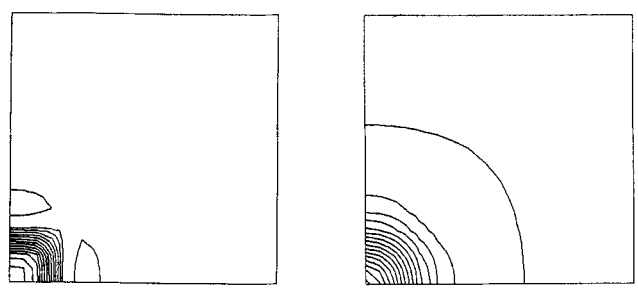

Figure 5. Pressure contours for the square jet

Flow past free running propellers[11]

In this section we consider the flow past a propeller in a free stream. Two cases are considered: a uniform flow and a shear flow.

Modelling of the propeller. The propeller is modelled by an actuator disc of radius equal to that of the propeller and of thickness roughly equal to the physical thickness of the propeller. The thrust and torque are allowed to vary in the radial direction but are constant in the peripheral direction. Little is known about thrust and torque distributions for a given propeller. For simplicity a simple trapezoidal distribution is used:

$$\begin{aligned} t(r) &= 0, && r \text{ in } [0, r_1], \\ t(r) &= t_m(r-r_1)/(r_2-r_1), && r \text{ in } [r_1, r_2], \\ t(r) &= t_m, && r \text{ in } [r_2, r_3], \\ t(r) &= t_m(R-r)/(r-r_3), && r \text{ in } [r_3, R], \end{aligned}$$

where t_m is the maximum value of the thrust and R is the radius of the propeller. Values of r_1, r_2 and r_3 were set to $0{\cdot}25R$, $0{\cdot}7R$ and $0{\cdot}85R$ respectively. These result in distributions similar to those predicted by simple propeller performance analysis. The same form is adopted for the distribution of the forces producing swirl. Its maximum value is denoted by s_m. The thickness of the propeller in this case is 0·041 propeller diameters. These distributions are integrated over the volume of the propeller to yield the global thrust and torque of the propeller:

$$T = 0{\cdot}3075 \times 2\pi \times R^2 \times t_m,$$
$$Q = 0{\cdot}2218 \times 2\pi \times R^3 \times s_m.$$

Given values of T and Q, t_m and s_m are computed, thus completing the definition of thrust and torque distributions.

Initial value of the eddy viscosity. The flow upstream of the propeller is undisturbed because there are no solid walls nor aftbody present. This makes the determination of the initial value of the eddy viscosity by classical boundary layer theory impossible. In References 9 and 10 and *ad hoc* procedure was used to initialize the turbulence model, but the authors stressed the need for a procedure based on sounder physical principles.

The flow through and past propellers has many of the characteristics of a turbulent jet or wake behind a streamlined body.[14,21] Hence an indication of the magnitude of the eddy viscosity can be obtained from a classical formula for jets:

$$\nu_T = 0{\cdot}025\, r_{1/2}\, \Delta U,$$

where $r_{1/2}$ is the half-width of the jet and can be taken here as $r_{1/2} = R$, the radius of the propeller (numerical experiments confirmed the validity of this assumption), and ΔU is the characteristic velocity excess.

A simplified one-dimensional analysis of inviscid flow past propellers[22] provides an estimate of this velocity excess. Figure 6 illustrates a propeller, with projected area A, immersed in a fluid with uniform velocity V_1. The speed of the fluid increases from V_1 to V_4 within the slipstream boundary. The relationship between thrust and velocity can be obtained from a momentum balance on the control volume S_6:

$$T = A(p_3 - p_2),$$

where p_2 and p_3 are the pressures at points 2 and 3; see Figure 6. Bernoulli's equation is not valid between points 1 and 2; however, it is applicable between points 1 and 2, and between 3 and 4. If points 1 and 4 are far away from the propeller, one can assume that $p_1 = p_4$ and write

$$T = \rho(V_4^2 - V_1^2)A/2$$

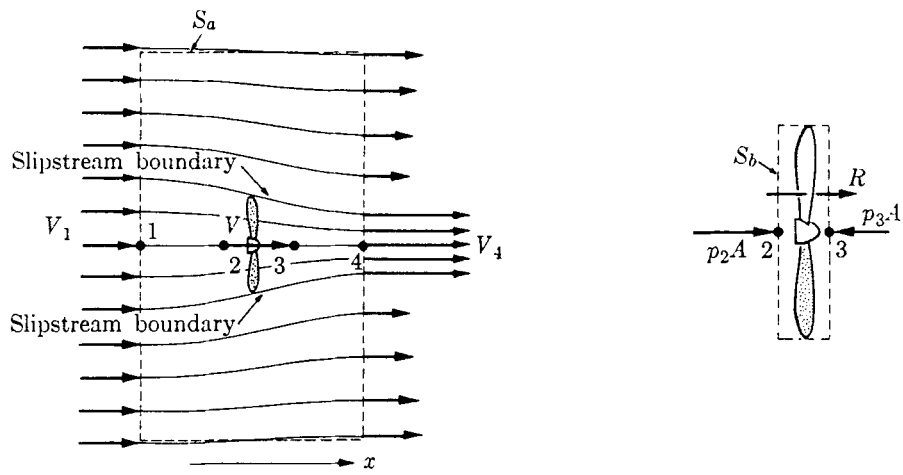

Figure 6. Simplified one-dimensional propeller analysis

or

$$V_4 = (2T/\rho A + V_1^2)^{1/2}$$

and the velocity excess is finally given by

$$\Delta U = V_4 - V_1.$$

The following data apply to the uniform flow case treated in Reference 23:

$$R^* = 0{\cdot}246 \text{ m},$$
$$U_0^* = 8{\cdot}52 \text{ m s}^{-1},$$
$$T^* = 2{\cdot}914 \text{ N},$$
$$A^* = 0{\cdot}19 \text{ m}^2,$$
$$\rho^* = 1{\cdot}177 \text{ kg m}^{-3},$$

yielding

$$\Delta U^* = 1{\cdot}41 \text{ m s}^{-1}$$

and a rough estimate of the eddy viscosity downstream of the propeller of

$$\nu_T^* = 0{\cdot}0087 \text{ m}^2 \text{ s}^{-1}$$

or in dimensionless form

$$\nu_T = 0{\cdot}002.$$

Upstream of the propeller the flow is nearly uniform and velocity gradients are small. Hence one expects the eddy viscosity to be nearly constant and small with respect to its value downstream. At some point just upstream of the propeller the velocity gradients becomes significant and the production of TKE increases, causing a smooth increase of the eddy viscosity through and past the propeller. The eddy viscosity continues its increase behind the propeller because pressure relaxation enhances the acceleration of the fluid. At some point downstream viscous dissipation causes stabilization of the value of the eddy viscosity.

There remains to select an initial value for the eddy viscosity. Obviously the initial value must be much smaller than found downstream. Assuming that the Prandtl–Kolmogorov relationship

holds we have

$$\nu_T = c\, k^{1/2} r_{1/2}.$$

Choosing $r_{1/2} = R$, $c = 0{\cdot}2$ from the jet value and $k = 0{\cdot}01\, U_0^2$ from Reference 23 we get the following estimate for the dimensionless initial eddy viscosity

$$\nu_{T0} = 0{\cdot}001.$$

To assess the validity of this analysis and the effect of the initial value of the eddy viscosity, axisymmetric simulations without swirl were performed on the uniform flow case of Reference 23. A mesh of quadratic elements extends from 4 diameters upstream of the propeller to 14 diameters downstream. In the radial direction it covers the region from the axis to 1·2 diameters in the free stream. This grid was obtained after several trials to ensure grid-independent solutions. All variables were non-dimensionalized with respect to the propeller diameter and the uniform upstream approach velocity. Uniform flow is enforced at the upstream boundary by setting $U = 1$ and $V = 0$. Symmetry is applied on the axis. On the free stream boundary $U = 1$ and the radial traction is set to zero. At the outflow both traction components vanish (Figure 7).

In all calculations the eddy viscosity solver was turned on at the first axial station where the maximum velocity excess was larger than 3% of the approach velocity. Figure 8 shows the distribution of eddy viscosity for various initial values in the range 10^{-5} to 4×10^{-3}. Values in the range 10^{-5} to 10^{-3} produce similar distributions with a peak value of 0·0025, a value in excellent agreement with the rough estimate of 0·002. The model is quite robust, since even for initial values that are not small compared with the downstream value, it tends to bring the eddy viscosity towards the value expected from the simple analysis.

An initial value of 5×10^{-4} was judged adequate. Simulations were performed with smaller initial values with little effect on the velocity and pressure fields.

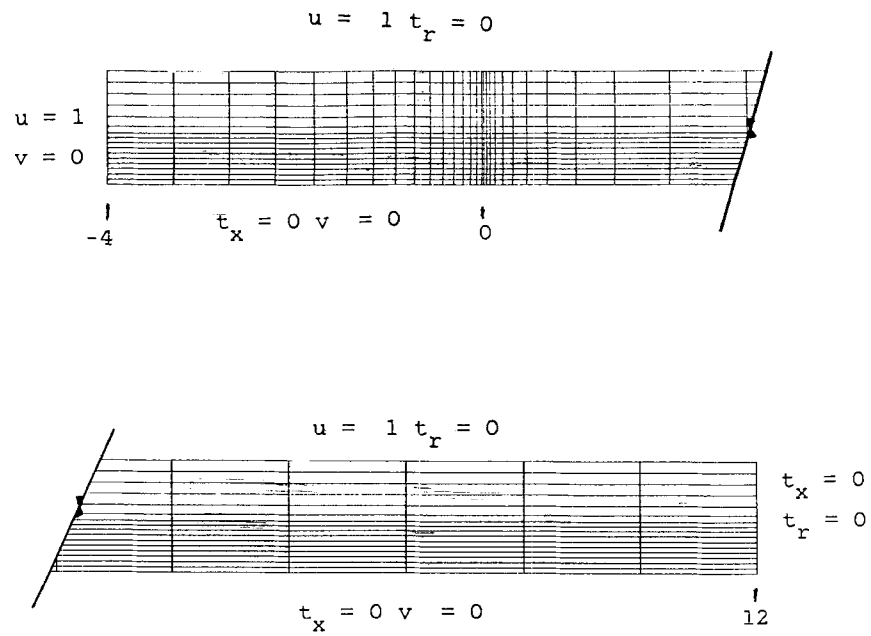

Figure 7. Mesh for tests on initial value of ν_T

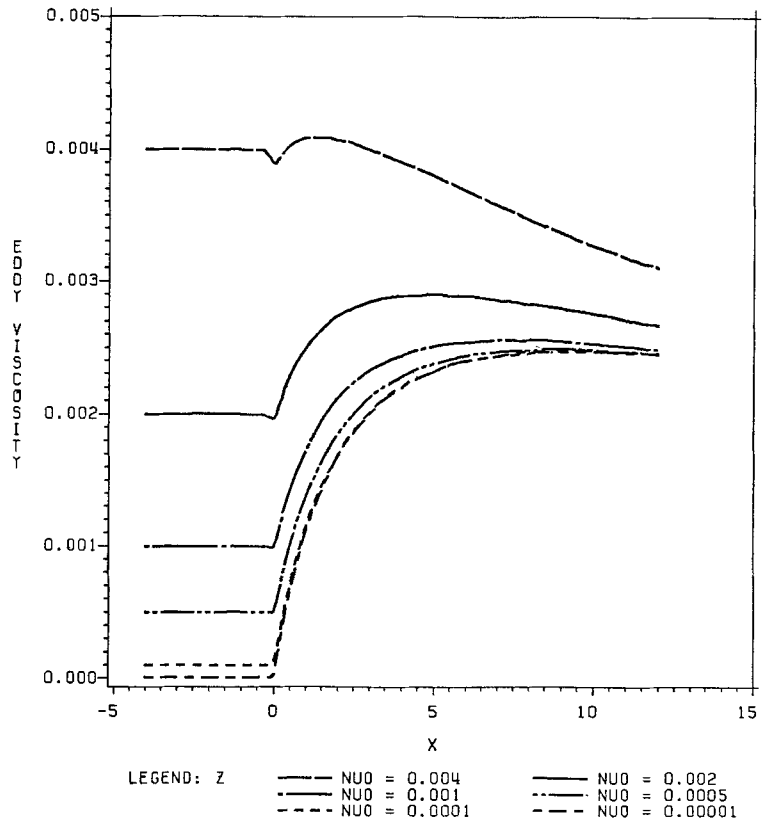

Figure 8. Effect of initial value of eddy viscosity

Uniform flow past a propeller.[11] The characteristics of the flow are[15,23]

$$U_0^* = 8{\cdot}53 \text{ m s}^{-1}, \qquad \rho_0^* = 1{\cdot}197 \text{ kg m}^{-3}.$$

The grid is a cylinder with 24 nodes in the axial direction, 14 radial nodes and 12 peripheral planes (see Figure 9). The inflow is located 2 diameters upstream of the propeller and the outflow at 3 diameters downstream. The free stream boundary is a shell of radius equal to 1·2 propeller diameters.

At the inflow U is set to one and V and W are set to zero. On the free stream shell U is set to one and the y and z tractions to zero. The three tractions are set to zero at the outflow. This results in a mesh with 3768 nodes and 3588 elements. There are 10 577 equations, and the matrix had 10 997 103 coefficients and a half-bandwidth of 521.

Mean flow quantities are not predicted or measured with the same accuracy. The velocity prediction is more accurate than that of the pressure. For experiments Kotb[23] reports that the order of decreasing accuracy is: axial velocity, pressure, swirl and radial velocity.

It should also be noted that while the finite element simulations can accurately represent a free running propeller, the experiment must use a shaft to support and drive the propeller. A body is placed close downstream of the propeller to house the drive train.[23] The housing affects the flowfield. The housing is located at 0·23D from the propeller and measurements were taken at

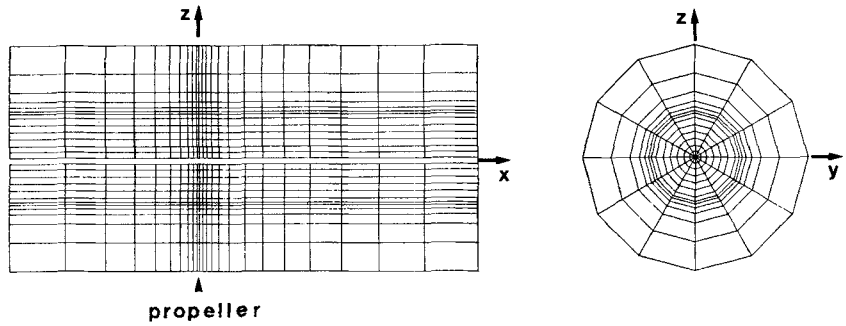

Figure 9. Grid for free shear flow near a propeller

0·025D and 0·23D downstream of the propeller. One should expect some discrepancies between predictions and experiments at 0·23D.

Figure 10 presents comparisons of experimental and predicted swirl and pressure. The agreement is excellent at $x/D = 0{\cdot}025$ and good at $x/D = 0{\cdot}23$. The quality of the prediction of swirl should be viewed as a major improvement over those of previous work.[9,10] The pressure prediction was the first one to be produced for such problems. The agreement is good at the first station. The disagreement at $x/D = 0{\cdot}23$ was caused by the disturbance due to the drive housing.[11]

Shear flow past a propeller.[11] The previous flow was in fact axisymmetric, although a 3D analysis was performed. The shear flow is a problem with truly three-dimensional features. The flow conditions are

$$U^*_\infty = 8{\cdot}52 - 0{\cdot}67y \text{ m s}^{-1}, \qquad U_\infty = 1 - 0{\cdot}1588y,$$
$$\rho^*_0 = 1{\cdot}77 \text{ kg m}^{-3}, \qquad D^* = 0{\cdot}492 \text{ m}.$$

To obtain the initial guess of the velocity field, an axisymmetric solution was obtained for a uniform flow and the velocity excess was extracted, rotated and added to the approach shear flow.

Figure 11 compares prediction and experiments. Here again the prediction is excellent for $x/D = 0{\cdot}025$ and good at $x/D = 0{\cdot}23$. Detailed study and analysis of the flowfield can be found in Reference 11.

Flow past a screen–propeller combination[24]

The goal of this simulation was to study the detailed 3D flowfield produced by a propeller operating in a 3D approach flow representative of real flows encountered in pusher–prop arrangements on aircraft or underwater vehicles; see Figure 12. Details of the experiments are contained in Reference 2. More detailed results of the simulations can be found in Reference 24.

The non-uniform inflow studied was generated by a varying mesh screen disc that consisted of one 0·38 m diameter mesh, one 0·13 m diameter mesh and a 30° wedge. Each screen had different size wires and spacing, creating screen regions with differing blockage factor.

The screen–propeller configuration of this section represents a considerable step in complexity. It is similar to the wake behind a slender body with a planar appendage. The flowfield is more complex, requiring careful consideration of grid requirements. It was also found necessary to extend the turbulence model to provide acceptable prediction. Lastly, the propeller disc loading was higher than in the previous cases.

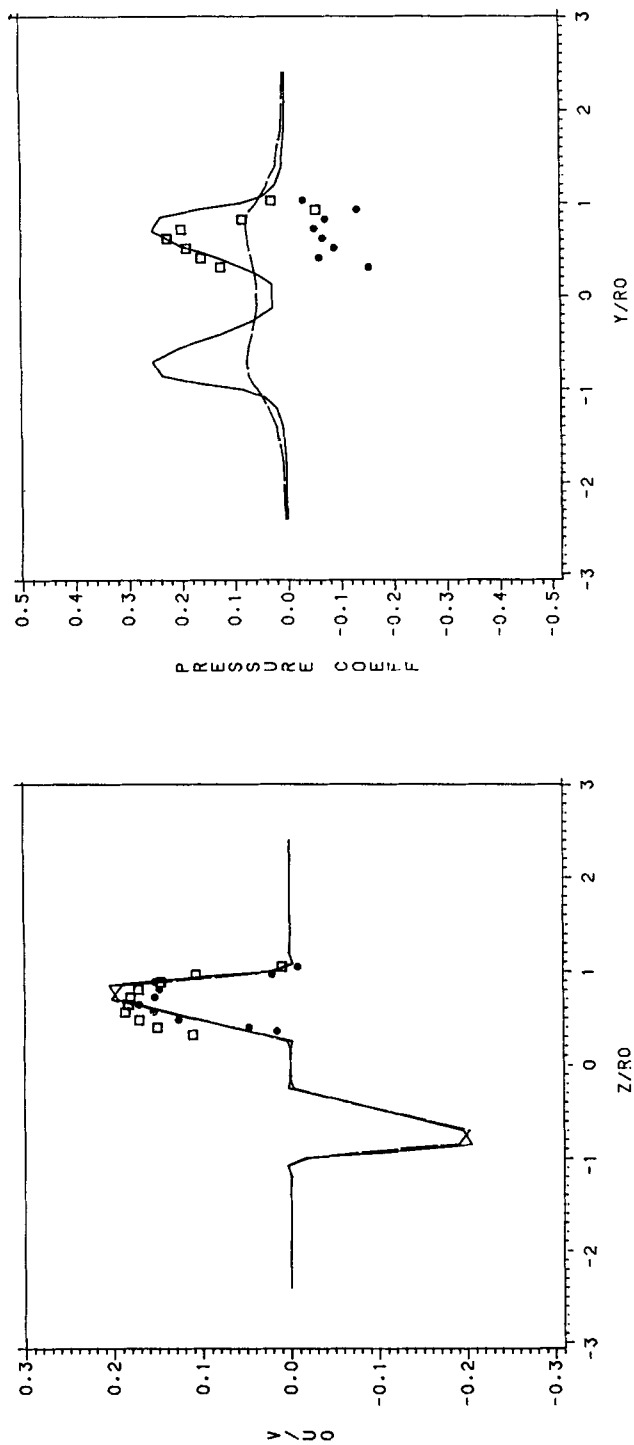

Figure 10. Predictions for propeller in uniform flow

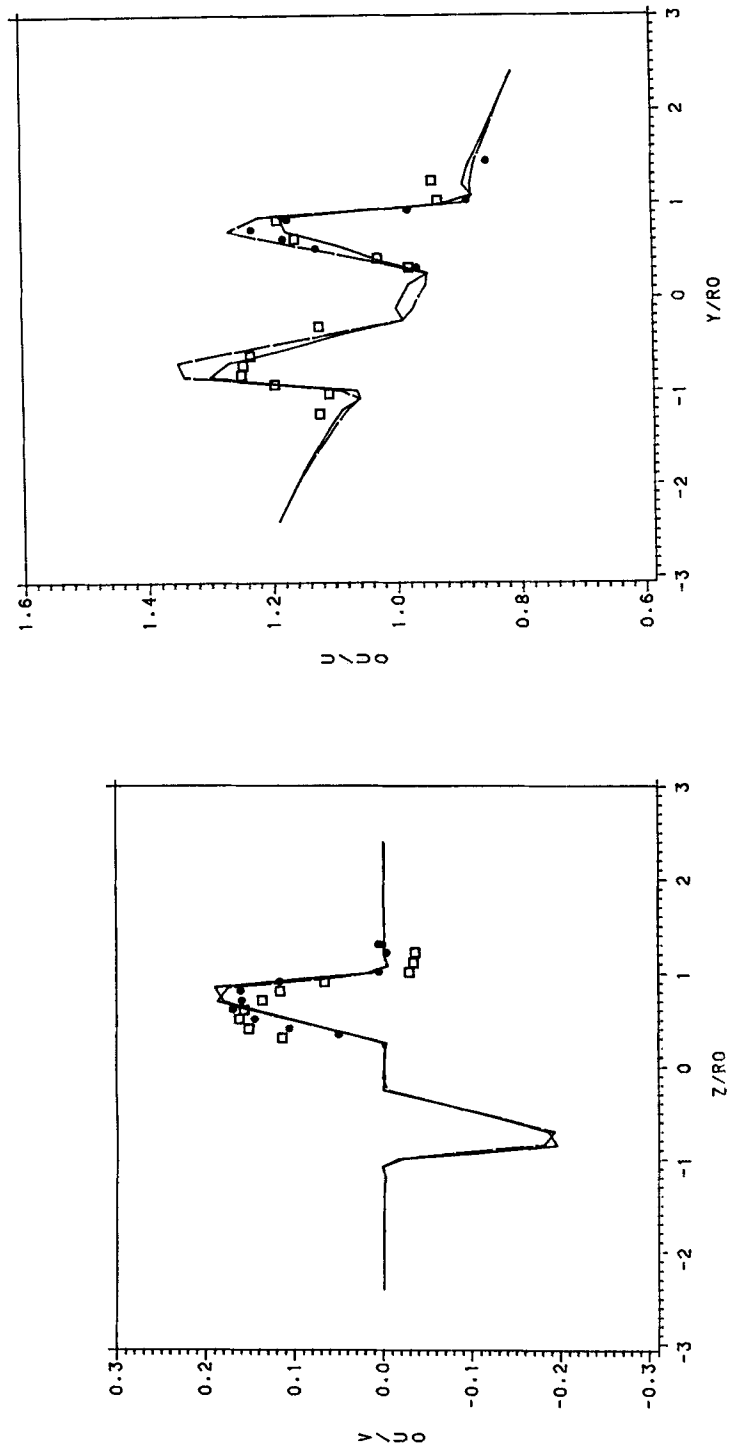

Figure 11. Predictions for propeller in a shear flow

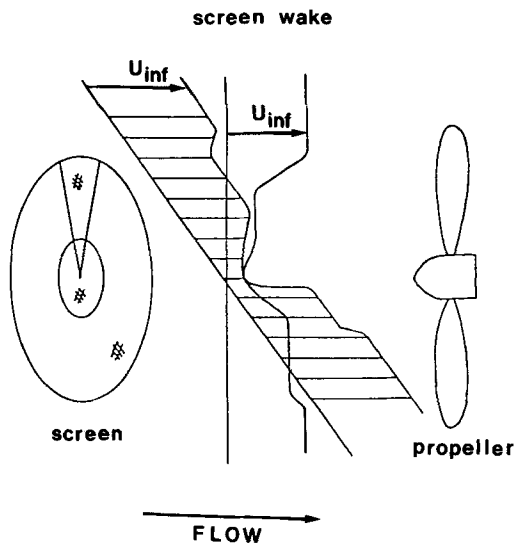

Figure 12. Non-uniform approach flow imposed by screen on the propeller

Modelling of the propeller and screen disc. The propeller is represented by the same actuator disc model. The effects of the screen on the flow are modelled in a similar fashion except that only axial forces are involved since the screen only produces drag. The analysis of Reference 26 is used to predict the local distribution axial force over the disc area. Because of the arrangement of the screen, this force varies both radially and tangentially.

Reference 26 gives a coefficient K related to the pressure drop through the screen as

$$\Delta P/(\rho U^2/2) = K\,(U_\infty/U_\infty)^2, \tag{11}$$

where U_m is the velocity just after the screen and

$$K = 0{\cdot}8\,S/(1-S)^2, \tag{12}$$

where S is the screen blockage. Finally we also have

$$U_f/U_\infty = (4-K)/(4+K), \tag{13}$$

where U_f is the velocity far behind the screen after the pressure has relaxed. Also one can show that

$$U_f - U_\infty = 2(U_\infty - U_\infty).$$

Combining these relationships we obtain an expression for the pressure drop across the screen which is related to the axial body force required for the finite element model:

$$\Delta P = f_x(r, \theta)/\Delta A = K(r, \theta) \times 1/2 \times \rho \times U_m^2. \tag{14}$$

Extension of the turbulence model. For the present flow problem it was found necessary to extend the basic model to cover the type of velocity profiles found behind the mesh screen. Because of the two mesh discs and the wedge, velocity profiles behind the screen exhibit significant variations. Consider a profile such as shown by the squares in Figure 13. Such a profile with visible plateau really has two mixing layers: an inner core up to the plateau and an outer layer between the plateau and the free stream.

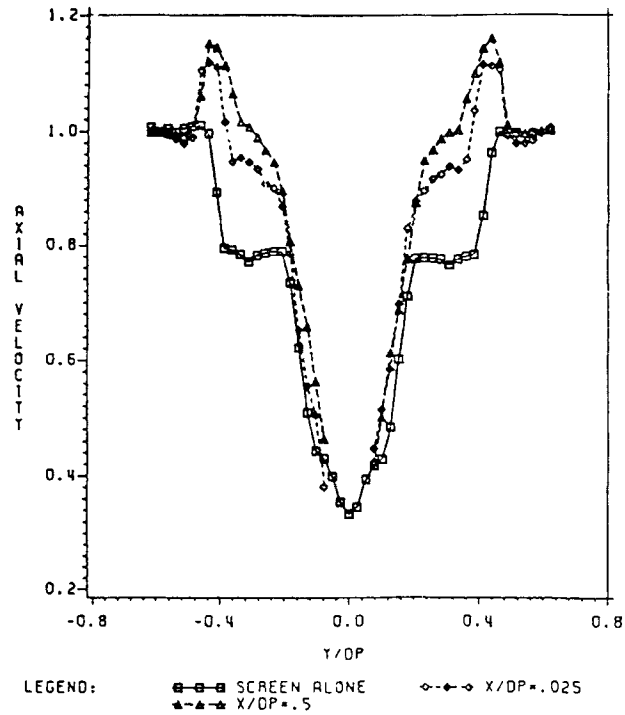

Figure 13. Mean axial velocity profiles downstream of the screen

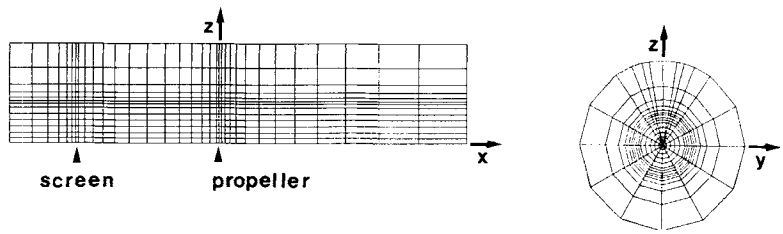

Figure 14. Grid for the screen–propeller combination

If equation (6) is used to determine the length scale, as is the practice for simpler wake and jet cases, too large an eddy viscosity will result. To handle such cases more adequately, the length scale subroutines of EDDY3D were enhanced to search for any plateau in the velocity profile. If a plateau is found, the half-widths are found using the value of $U_{\text{plat.}}(x)$ in place of U_∞ in equation (6); if not, equation (6) is used. All other features of the model are unchanged.

Results for the screen–propeller combination. The grid used is shown in Figure 14. There were 38 sections in the axial direction, 15 nodes in the radial direction and 18 nodes in the peripheral direction. The grid had to be refined to resolve the sharp gradients expected at the edge of the screen wedge. Cross-sections were clustered near the screen and around the propeller rotor locations. This resulted in 9072 elements and 9361 nodes. There were 26 676 equations and

43 727 562 coefficients in the matrix with a half-bandwidth of 820. The solution required five quasi-Newton iterations to reach a convergence of 0·01 on the relative changes in the velocity and residual vectors; 327 minutes of IBM-3084 were needed to complete the simulation. The initial guess of solution was taken as an axisymmetric solution without swirl. In the axisymmetric model the wedge could not be accounted for; its effect is only felt in the 3D model.

The initial value of the eddy viscosity was taken as 5×10^{-5}. Care must be used in selecting this value. It must be small enough compared with the expected values in the main turbulent region. It cannot be zero or too small, because then the equations of motion approach the inviscid Euler equations, which cannot be handled by FIDAP.

The predictions for the axial velocity along horizontal and vertical traverses at $x/D = 0{\cdot}025$ and $x/D = 0{\cdot}5$ are compared with the data in Figure 15. All of the main features of the flow are captured and the quantitative agreement is quite good. Experiments show considerable changes in the velocity profiles in going from $x/D = 0{\cdot}025$ to $0{\cdot}5$,[25,26] and the numerical predictions correctly model that behaviour as can be seen from Figure 15. Any objective judgement of these comparisons would have to conclude that the agreement shown here is as good as or better than is common for 2D turbulent free shear flows,[14] no less for a truly 3D case such as here.

Swirl predictions are compared with the experiments in Figure 16. The slight discrepancy in the location of the peak is the result of the simple assumption for the radial distribution of the torque. This particular variation was selected prior to both the experiment and the calculation based only on what seemed reasonable. Obviously some further adjustment of the variation would improve the comparison, but such a procedure was judged as not being strictly honourable and was not done. To put the agreement achieved here in perspective, it is a little poorer than that achieved for uniform and linear shear flows but much better than that found for the axisymmetric flow behind a slender body with a propeller.[9,10]

Some comparisons of radial velocity predictions are included in Figure 17. This component is very small and difficult to measure; hence there is scatter in the data but the predictions have to be rated as being good. This is noteworthy, since other workers have often reported poor predictions of the radial velocity component with the elaborate inviscid codes.

CONCLUSIONS

This work has presented a general purpose, advanced computational technique for three-dimensional turbulent free shear flows. The turbulence model was successfully applied, within a finite element framework, to several problems, demonstrating the general applicability, robustness and flexibility of the finite element method for solving complex three-dimensional turbulent flows. The main results can be summarized as follows:

(1) Predictions are in good agreement with experiments for the square jet problem.
(2) The simple turbulence model presented here produced predictions for uniform and shear flows and the more complex upstream inflow into a propeller which show very good agreement with the data for the axial and swirl components of velocity.
(3) The numerical simulations show that the propeller exerts a strong upstream influence on the axial and radial velocity fields and on the pressure field. Only an elliptic formulation such as that of FIDAP can correctly reproduce these physical effects.
(4) The combination of the turbulence model and the Galerkin finite element algorithm of FIDAP is robust and stable, mostly due to the full coupling of the momentum and continuity equations. The complex features of the flow were captured. No gradual introduction of the propeller loading as the iteration proceeds is required, in contrast to some previous works.

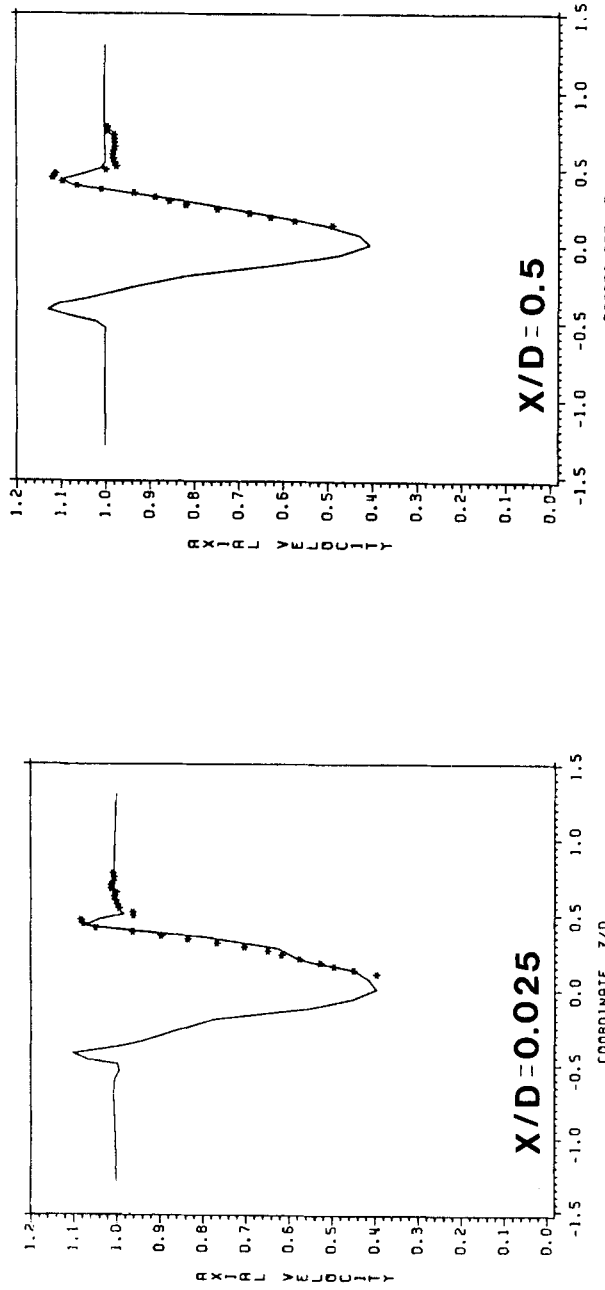

Figure 15. Screen–propeller: axial velocity

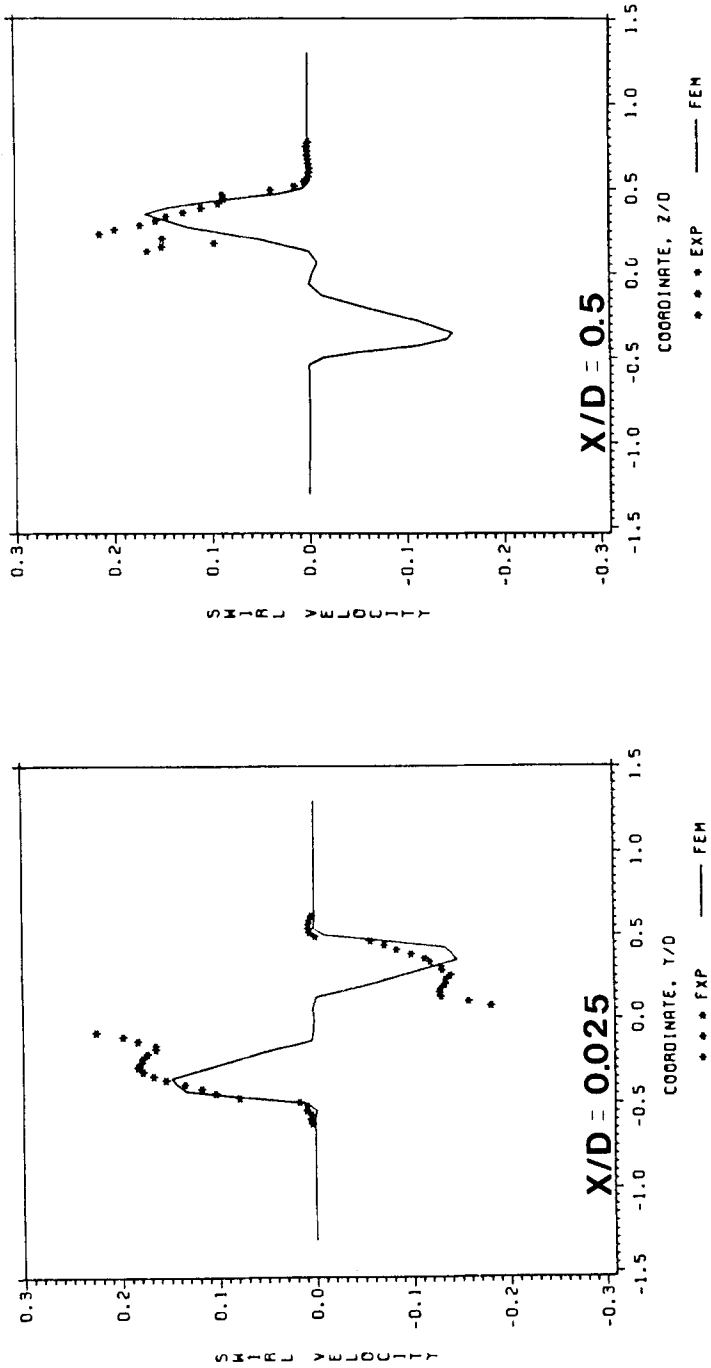

Figure 16. Screen–propeller: swirl velocity

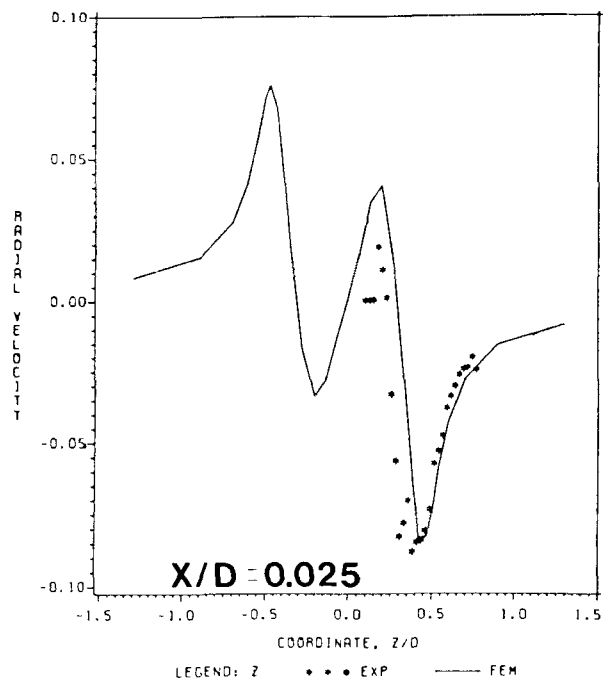

Figure 17. Screen–propeller: radial velocity

(5) The current simple approach to interfacing the turbulence model with FIDAP is probably not optimal, but it proved quite flexible in following the various releases and updates of the package.

Current efforts using FIDAP involve the solution of a three-dimensional body–propeller combination. Preliminary results are very encouraging. The presence of the hull introduces new complexities in the turbulence model and stronger non-linearities, making such simulations quite expensive. Nevertheless, such an approach seems the only viable one to obtain solutions to such problems. Results from these simulations are incomplete at this time and will be reported in a forthcoming publication.

Another application of the FIDAP concerns the solution of the 3D turbulent flowfield near individual propeller blades. In a first step excellent results were obtained for the flow past a 3D finite flat plate.[27]

NOMENCLATURE

a	exponent
A	cross-section of the flowfield, area of the propeller
a_2	constant in turbulence model
c_2	constant in turbulence model
D	domain of solution and propeller diameter
f_1	body force
k	turbulence kinetic energy

K	screen coefficient
L	length scale
Q	torque of the propeller
r	radial co-ordinate
$r_{1/2}$	half-width of the shear layer
R	propeller radius
s	radial distribution of swirl force
S	screen blockage
t	radial distribution of thrust
$\mathbf{t}_1$	surface traction vector
T	thrust of the propeller
U_c	centreline velocity
U_f	velocity far behind the screen
$\mathbf{U}_i$	velocity vector
U_s	velocity just behind the screen
U_∞	upstream approach flow
x_i	co-ordinates
$Y_{1/2}$	half-width of the shear layer
$Z_{1/2}$	half-width of the shear layer
ρ	density of the fluid
ε	turbulence viscous dissipation
μ_T	eddy viscosity
ν_t	kinematic eddy viscosity
γ	eddy viscosity distribution function

REFERENCES

1. J. A. Sparenberg, 'On the potential theory of the interaction of an actuator disk and a body', *J. Ship Res.*, (December 1972).
2. J. A. Sparenberg, 'On the linear theory of an actuator dusk in a viscous flow', *J. Ship Res.* (March 1974).
3. J. E. Kerwin, 'Prediction field point velocity program (MIT-FVP-10)', MIT, December 1979.
4. D. L. Whitfield and A. Jameson, 'Three dimensional Euler equation simulation of propeller–wing interaction in transonic flow', *AIAA Paper 83-0236*, 1983.
5. L. J. Bober, D. S. Chaussee and P. Kutler, 'Prediction of high speed propeller flow fields using a three-dimensional Euler analysis', *AIAA Paper 83-0188*, January 1983.
6. J. M. Barton, O. Yamamoto and L. J. Bober, 'Inviscid analysis of advanced turboprop propeller flow fields', *AIAA Paper 85-1263*, July 1985.
7. N. J. Yu and H. C. Chen, 'Flow simulations for nacelle–propeller configurations using Euler equations', *AIAA Paper 84-2143*, August 1984.
8. W. O. Valarezo and J. L. Hess, 'Time-averaged subsonic propeller flowfield calculations', *AIAA-86-1807-CP*, 1986.
9. J. A. Schetz and S. Favin, 'Numerical solution for the near wake of a body with propeller', *J. Hydronautics*, **11**, (October 1977).
10. J. A. Schetz and S. Favin, 'Numerical solution of a body–propeller combination flow including swirl and comparison with data', *J. Hydronautics*, **13**, (April 1979).
11. D. H. Pelletier and J. A. Schetz, 'Finite element Navier–Stokes calculation of three-dimensional turbulent flow near a propeller', *AIAA J.*, **24**, (September 1986).
12. W. Rodi, *Turbulence Models and Their Applications in Hydraulics*, International Association for Hydraulic Research, Delft, 1980.
13. T. Cebici and P. Bradshaw, *Momentum Transfer in Boundary Layers*, Hemisphere, McGraw-Hill, 1977.
14. J. A. Schetz, *Injection and Mixing in Turbulent Flow; Progress in Astronautics and Aeronautics, Vol. 68*, AIAA, New York, 1980.
15. D. H. Pelletier 'Finite element solution of the Navier–Stokes equations for 3-D turbulent free shear flows.' *Ph.D. Dissertation*, Aerospace and Ocean Engineering Department, Virginia Polytechnic Institute and State University, Blacksburg, VA, October 1984.
16. P. M. Sforza, M. H. Steiger and N. Trentacoste, 'Studies on three-dimensional viscous jets', *AIAA J.*, **1**, (1966).

17. J. J. McGuirk and W. Rodi, 'The calculation of three-dimensional free jets', *Turbulent Shear Flows I*, Springer-Verlag, 1979.
18. J. O. Hinze, *Turbulence*, 2nd Edn, McGraw-Hill, New York, 1975.
19. M. P. du Plessis, R. L. Wang and R. Kahawita, 'Investigation of the near region of a square jet', *Trans. ASME, J. Fluids Eng.* (September 1974).
20. H. Schlichting, *Boundary Layer Theory*, 7th Edn, McGraw-Hill, 1979.
21. J. A. Schetz, *Foundation of Boundary Layer Theory for Momentum, Heat, and Mass Transfer*, Prentice-Hall, 1984.
22. W. H. Li and S. H. Lam, *Principles of Fluid Mechanics*, Addison-Wesley, Reading, MA, 1964.
23. M. Kotb, 'Experimental investigation of 3-D turbulent free shear flows past propellers and windmills', *Ph.D. Dissertation*, Aerospace and Ocean Engineering Department, Virginia Polytechnic Institute and State University, Blackburg, VA, October 1984.
24. J. A. Schetz, D. Pelletier and D. A. Mallory, 'Numerical and experimental investigation of a propeller flowfield with a 3-D non-uniform inflow', *AIAA Paper 87-0607, AIAA 25th Aerospace Sciences Meeting*, Reno, Nevada, 2–15 January 1987.
25. D. A. Mallory, 'Experimental investigation of non-uniform flow past propellers', *M.S. Thesis*, Virginia Polytechnic Institute and State University, 1985.
26. G. I. Taylor, 'Air resistance of a flat plate of very porous material', *Aeronaut. Res. Council Rep. Memo. 2236*, 1944.
27. J. Caille and J. A. Schetz, 'Finite element Navier–Stokes analysis of the flow about a finite flat plate', *Paper AIAA-87-1422, AIAA 19th Fluid Dynamics, Plasma Dynamics and Lasers Conf.* Honolulu, Hawaii, 8–10 June 1987.